Shape- and polymer-considered simulation to unravel the estuarine microplastics fate

Yichuan Zeng[a, b, 1], Hua Wang[a, b, 1, *], Dongfang Liang[c], Weihao Yuan[d], Yuhan Shen[e], Zilin Shen[a,b], Qihui Gu[a,b]

a. Key Laboratory of Integrated Regulation and Resource Development on Shallow Lake of Ministry of Education, College of Environment, Hohai University, Nanjing 210098, China.

b. College of Environment, Hohai University, Nanjing 210098, China.

c. Department of Engineering, University of Cambridge, Cambridge CB2 1PZ, UK.

d. Nanjing Institute of Environmental Science, Ministry of Ecology and Environment, Nanjing, 210042, China

e. Dept. of Civil, Environmental and Geomatic Engineering, University College London, London WC1E 6BT, UK

***Corresponding author:** Hua Wang; E-mail: wanghua543543@163.com.

[1] Yichuan Zeng and Hua Wang contributed to this work equally.

Abstract: Environmental microplastics (MPs) constitute various sizes, polymers, and shape components. In estuaries, such differences are related to the reliability of assessing the seaward fate of MPs, aggregation hotspots, and ecological risks. This study sets the MP particle mass gradient using the shape factor and size probability density function to categorically estimate the MP load in the surface layer of the Yangtze River Estuary (YRE), which is the largest contributor of plastics to the sea. During the high plastic input period in July, the optimized estimated MP load through the surface layer of the YRE was 9766 kg/month, which was overestimated by 821 kg/month based on the empirical average particle mass. While tracking MP transport classified by shape and polymer type, the resuspension of MPs that accumulate in the intertidal zone cannot be neglected. The average relative error of the simulation was as low as 19.6% after including the abovementioned factors. Finally, the simulation results of the sensitive regions were extracted to assess the new MP risk index, which considers shape, abundance, and polymer type. By introducing

these essential tools, this study helps to understand the fate of riverine MPs entering estuaries, where valuable opportunities for removing MPs exist before they spread to the oceans.

Keywords: microplastic fate; classified simulation; size probability density function; particle shape; polymer type

1. Introduction

Nearly 60–80% of synthetic plastic products have been discarded since humans began to embrace plastic in the 1950s (Geyer et al., 2017; Meijer et al., 2021). Discarded plastics in the environment are fragmented by natural forces and, together with a minority of primary microplastics (MPs) (Boucher and Friot, 2017), constitute the sources of environmental MPs (1–5000 μm). Despite undergoing the processes of settling, deposition, and accumulation (Ceccarini et al., 2018; Hurley et al., 2018; Woodward et al., 2021), more than 50% of environmental MPs (4.8–12.7 million MT/a) reach the sea through riverine transport and coastal emissions (Jambeck et al., 2015; Wang et al., 2022). Therefore, estuaries act as terminal gateways for terrestrial MPs. The 'estuarine filter' triggered by tide-runoff interactions (Celis-Hernandez et al., 2021; Durr et al., 2011) features significant MP input accumulation and output lags. For example, estuarine surface fronts with acute density gradients (Corlett and Geyer, 2020; Odonnell, 1993) are major aggregation hotspots that mitigate MP transport to the ocean (Wang et al., 2022).

Until environmentally friendly alternatives to plastics are invented, the abundance of plastic debris and the proportion of small particle sizes will continue to increase. The ingestion of micro/nanoplastics with trapped bacteria (Akhavan et al., 2011) by aquatic organisms (Besseling et al., 2019) and bioaccumulation through food webs (MacLeo et al., 2021) constitute the adverse effects of environmental MPs on life health risks, such as reproductive disturbance (Akhavan et al., 2015; Jin et al., 2022), inhibition of nerve conducting enzyme activity (Yin et al., 2021), and oxidative stress (Schirinzi et al., 2017). Moreover, the random leaching risk of plastic additives carried by environmental MPs (Hermabessiere et al., 2017; Koelmans et al., 2017; Wiesinger et al., 2021) is severe. Hence, improved recognition of estuarine MP transport simulations is needed to develop a more effective removal strategy before MP accumulation hits global marine ecosystems.

Existing transport simulations employ buoyant particles to represent the common MP type (Cohen et al., 2019;

Onink et al., 2021) and derive valuable insights into the controlling parameters, such as shape (Waldschlaeger and Schuettrumpf, 2019), density (Collins and Hermes, 2019), biofilm (Rummel et al., 2017), and aggregation behavior (Andersen et al., 2021) on particle transport. However, these buoyant particles are a simplified form of MP particles, and their use for simulations results in gaps in the understanding: first, the uniform particle mass ignores the particle size and polymer diversity, producing notable biases in estimating MP loads and abundances from riverine inputs to the ocean. Second, current simulations present the total MP distribution but lack subclassifications such as shape and polymer type, which can affect MP transport through settling, dispersion, and bioavailability. Therefore, this study made three key adjustments to traditional transport simulations of MP transport in the Yangtze River Estuary (YRE) with the aim of filling these gaps: (1) MP loads through the surface layer of the YRE were modified by replacing mean particle mass with the mass gradient through MP size probability density function (Kooi et al., 2021); (2) the transport of main MP types was distinguished via a new shape factor (Zhang and Choi, 2022); and (3) for East Asian rivers, the MP sources during the high plastic input season (July to August) (Lebreton et al., 2017) should contain the resuspension of MPs accumulated on the intertidal zone since dry season. The improved model developed in this study can be used to produce improved MP transport simulations and help inform the management of estuarine MPs.

2. Methodology

2.1 Study area

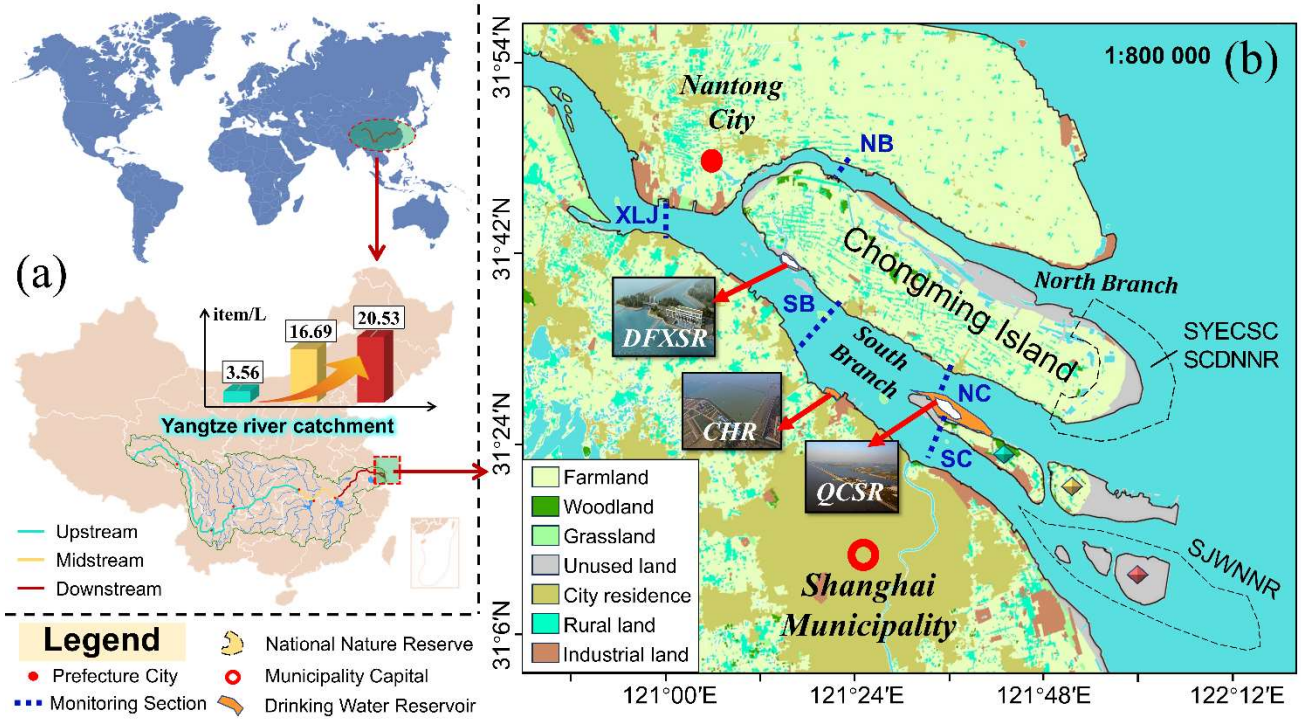

Fig. 1. Distribution of study area: (a) location of the Yangtze River catchment and microplastic (MP) abundance (item/L) and (b) distribution of six protected objects and land use in the Yangtze River Estuary.

The MP abundance in the world's largest plastic-contributing catchment (Lebreton et al., 2017), the Yangtze River catchment, shows an increasing trend from upstream to the estuary (Yuan et al., 2022) (Fig. 1a), whose high plastic input season (June to August) was regulated by the East Asian monsoon (Fig. 2a). Diverse land-use types across watersheds link heterogeneous pollution sources as significant anthropogenic triggers for the spatial variability of MPs and their occurrence in aquatic environments. Chongming Island divides the Yangtze River into the north branch (NB) and south branch (SB) starting at the Xuliujing (XLJ) section. At Changxing Island, the SB is further divided into the northern channel (NC) and southern channel (SC). These channels flow into three water sources that supply water to 25 million people in Shanghai: the Dongfengxisha Reservoir (DFXSR), Chenhang Reservoir (CHR),

and Qingcaosha Reservoir (QCSR). The highest MP concentration is found in the south SB and SC (i.e., Shanghai municipality) and is caused by heavy industrial land, followed by farmland, with residential areas being the lowest contributors (Fig. 1c) (Chen et al., 2020). Two overlapping nature reserves are located on the eastern side of Chongming Island: the Shanghai Yangtze Estuary Chinese Sturgeon Conservation (SYECSC), dedicated to providing a 'nursery' for juvenile Chinese sturgeon (Zhou et al., 2020), and the Shanghai Chongming Dongtan National Nature Reserve (SCDNNR), dedicated to protecting migratory birds.

2.2 Numerical simulation

2.2.1 Simulation scheme

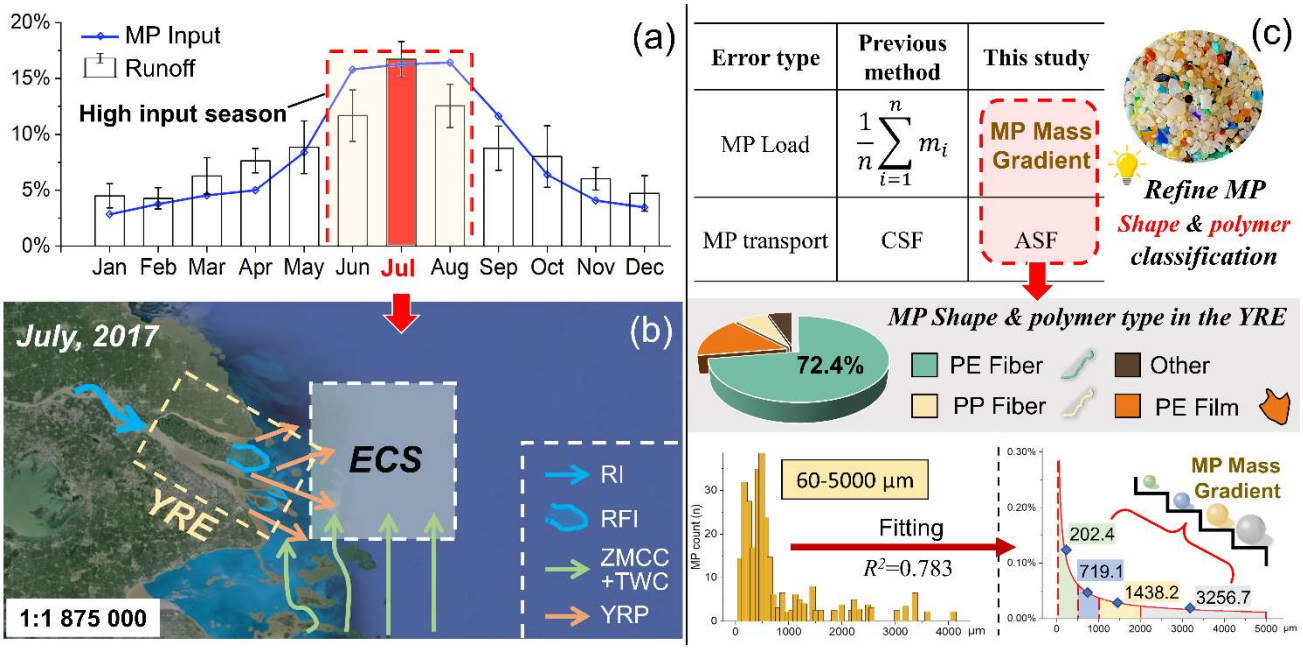

Fig. 2. Simulation scheme: (a) yearly percentage peak of runoff in the XLJ section (2015-2020) and seasonal plastic input to the ocean from the Asia rivers (Lebreton et al., 2017); (b) MP transport regulated by tide-runoff interaction of the YRE in summer. RI (riverine input), RFI (resuspension from the intertidal zone), ZMCC (Zhejiang and Fujian coastal current), TWC (Taiwan warm current), and YRP (Yangtze river plume). (c) Approach to reducing MP flux and transport errors by classifying them by polymer and shape and fitting a

probability density function to calculate the particle mass gradient.

We searched Web of Science for studies that investigated MPs in the surface waters of the YRE and found 11 retrievable papers. Of these, five (Table S1) were selected that documented detailed distribution data in the high plastic input season (Li et al., 2020b; Luo et al., 2019; Xu et al., 2018; Zhao et al., 2014; Zhao et al., 2019). The plastic identification of Zhao et al. (2014), based on visual inspection with an optical microscope, resulted in much higher abundance results than those of other studies and was thus excluded as an outlier. To improve the reliability of the size distribution by obtaining data from multiple sources, for the remaining four papers, the lower MP size limit was uniformly adjusted to 60 μm and the number of particles corresponding to the size fraction was normalized to a percentage. Additionally, 2017 was a normal water year from a precipitation perspective, according to the Shanghai Water Authority (Shanghai Water Authority, 2020). Therefore, July 2017 was selected as the representative simulated month in the high plastic input season for the largest global MP contribution (Fig. 2a, 2b). Combining the results of the four studies, the main MP types on the surface layer of the YRE were polyethylene fibers (PE fibers) > polyethylene films (PE films) > polypropylene fibers (PP fibers) (Fig. 2c), which together accounted for more than 94% of the total. Thus, these three MPs can capture the main characteristics of the MP community. This can be attributed to the propensity of small, low-density MPs to be governed by surface tension, resulting in their accumulation at the water surface. In deeper water layers, a higher proportion of larger-sized high-density MPs prevail, necessitating a reassessment of their distribution characteristics. In addition to riverine input, there is another seasonal MP source: an average of over 70% of MPs in spring were stranded in the southeastern intertidal zone of Chongming Island (Shen et al., 2022) and resuspended by surface currents (Onink et al., 2021). We set out three scenarios in Section 3.2 to demonstrate the necessity of considering the MP sources resuspended from the intertidal zone during summer and shape-dependent MP transport.

2.2.2 MP load modified by particle size probability density function

MP abundance is mostly characterized by the number per unit volume (N/m^3); therefore, an accurate riverine MP load is critical for converting abundance to mass concentrations. For YRE, the abundance in the 60–1000 μm range (filter pore size = 60 μm) accounts for >75% of the total, which is consistent with a heavy-tailed size distribution character of global MPs (Koelmans et al., 2022; Kooi and Koelmans, 2019). However, in estimating the MP load through the YRE, previous studies ignored the particle size distribution and randomly selected particles to take a mass average of 33 μg (Shen et al., 2022; Zhao et al., 2019). Using a uniform particle mass for the entire MP population may result in bias and should be corrected by calculating the mass gradient from the MP-size probability density function (PDF) (Fig. 2c). All the data from the four aforementioned studies were normalized to the percentage of the total number of particles in specific size fractions for comparability. Five distributional features were preset for fitting. After a goodness-of-fit test, the power function (Kooi et al., 2021) best fitted the relationship between grain size and abundance (R^2=0.783; Fig. 2c and Table S2).

The particle sizes were divided into four fractions: 60–500, 500–1000, 1000–2000, and 2000–5000 μm (the upper limit of MP). Since the longest (a), intermediate (b), and shortest lengths (c) of the particles are vital for estimating the particle volume, we derived the median particle size ($\bar{M}$) using the harmonic mean point of the power function (Table 1), regarded as the intermediate length (b) for each size fraction of the film and the longest length (a) for each size fraction of the fiber, to obtain the minimum volume error. Given the clear distinction in Aschenbrenner shape factor (ASF) for film MPs (most ASF<0.1), fragment MPs (0.1<ASF<1), and fiber MPs (ASF>1) (Zhang and Choi, 2022), we obtained the ASF from the MP shape database (Van Melkebeke et al., 2020) to approximate the particle shape. The equivalent volume diameter (D_{eqv}) of particles with different size fractions and polymer compositions, but the same shape (Fig. 2c), can be back-calculated in three steps: First, the ASFs of each shape in

the database were positively sorted to locate the median-belonging particle as the sample particle (SI 2). Second, because ASF and $\bar{M}$ are fixed, the remaining two lengths can be calculated in equal proportions to a, b, and c of sample particles with a typical shape (Eq. 5-4). Third, Eq. 3 was used to calculate the equivalent volume diameter (D_{eqv}) and the volume of the particles. The particle mass gradient was obtained by multiplying the densities and volumes of the different polymer types (Table 1).

We compared four studies (Table S3) that collected global riverine MP datasets and explicitly estimated the representative particle masses (Lebreton et al., 2017; Schmidt et al., 2017; Weiss et al., 2021; Zhao et al., 2019. Our calculated fiber mass satisfied the law that the fiber mass should be much lower than the nonfibrous mass; however, the representative mass of fibers in the dataset (7.5 μg/item) (Weiss et al., 2021) lay between the 2nd and 3rd fraction of our mass gradient. The core idea for upgrading MP simulations is to replace the average particle mass with the mass gradient classified by the polymer type and particle size. Considering that the MP distribution pattern is influenced by the Yangtze diluted water in summer (Peng et al., 2017), we first placed the MP emission sources in the SB and NB according to a runoff allocation ratio of 19:1 (Obodoefuna et al., 2020) to minimize the transport error. Scenario 1 employed the load by directly multiplying the empirical mean particle mass (33 μg), MP abundance, and hourly discharge. The only difference in Scenario 2 lies in setting the gradient and proportion of the particle mass with reference to Table 1.

Table 1. MP particle mass gradient classified by size, polymer, and shape factor in the surface layer of the YRE

MP type	Size fraction (μm)	Proportion of total	$\bar{M}$ (μm)	Equivalent volume (cm^3)	Particle mass (mg/item)	ASF of sample particle
PE fiber	60–500	42.97%	202.4	2.691E-08	2.64E-05	2.725
	500–1000	14.85%	719.1	1.208E-06	1.18E-03	
	1000–2000	9.73%	1438.2	9.661E-06	7.23E-03	
	2000–5000	8.95%	3256.7	1.122E-04	1.04E-01	

PE film	60–500	9.19%	202.4	1.344E-07	1.32E-04	0.033
	500–1000	3.18%	719.1	6.032E-06	5.90E-03	
	1000–2000	2.08%	1438.2	4.826E-05	3.61E-02	
	2000–5000	1.92%	3256.7	5.603E-04	5.21E-01	
PP fiber	60–500	4.00%	202.4	2.578E-08	2.53E-05	2.725
	500–1000	1.38%	719.1	1.157E-06	1.13E-03	
	1000–2000	0.91%	1438.2	9.254E-06	6.93E-03	
	2000–5000	0.83%	3256.7	1.074E-04	9.99E-02	

2.2.3 Parameterization of MP transport

2.2.2.1 MP property distinguished by polymer composition

MP particles suffer from fragmentation effects, such as photo-induced surface cracking and beach-based abrasion, with a minimum threshold of 2 months (Song et al., 2017) and a threshold of 3+ years for large-scale mass loss (Onink et al., 2022). In our one-month simulation period, MPs could be viewed as persistent particles from the perspective of their entire life cycle. Heterogeneous aggregation is a key identifier of MPs (Singh et al., 2019; Wang et al., 2021) and biofouling and flocculation of suspended sediments are the main pathways for aggregation (Long et al., 2017), which are related to the polymer composition of MPs. Biofilm formation on MP surfaces can be divided into reversible adhesion, irreversible adhesion, biofilm formation, shedding, and recolonization. In a past study, biofilms were observed on the surface of PP MPs within several days (Lagarde et al., 2016). However, it is difficult for PE MPs to flocculate or undergo biofouling (Lagarde et al., 2016; Li et al., 2019).

Given the above description and the polymer density, in our simulation PE MPs were considered buoyant particles without heterogeneous aggregation and settling and PP MPs were regarded as independent settling particles whose settling velocity follows biofilm growth. Previous studies have indicated that the thickness of biofilms growing on the same polymer type at specific times is similar, regardless of the MP size (Liu et al., 2022). The high flow rates downstream of the Yangtze River facilitate the growth of denser and thinner biofilms in summer (He et al., 2022; Zhang et al., 2021). We therefore classified four stages for the biofouling from scratch according to the MP biofilm

166 formation experiment of (Liu et al., 2022): days 0–6, no biofilm; days 6–12, 0.05 μm/d; days 12–24, 0.1 μm/d; days
167 24–31, 0.5 μm/d. The biofouling rate settings were based on empirical values from Jervis Bay (Jalon-Rojas et al.,
168 2019) and were applied to the biofilm volume calculation in Eq. 4.

169 **2.2.2.2 Tracking the transport of MP particles**

170 As the simulation fundament, the 3-dimensional incompressible Reynolds averaged Navier-Stokes equations
171 were used to explain estuarine hydrodynamic processes (DHI, 2017b). The path of the MP particles was calculated
172 using the output velocity of the hydrodynamic model. The fourth-order accurate Runge-Kutta method was used to
173 integrate the particle position equation (DHI, 2017a). Owing to the existence of current and random walk in the sub-
174 grid-scale diffusion process, the Rwpt model can be described as advection and reformulated as diffusion.

175 $$X^{t+\Delta t} = X^t + U\Delta t + R(t)\sqrt{2K_h\Delta t} \quad (1)$$

176 where X^t and $X^{t+\Delta t}$ are the passive particle position vector times of t and $t+\Delta t$, respectively; U is the
177 velocity vector of the model flow field; Δt is the time step of the random walk; $R(t) \in [-1,1]$ is a uniformly
178 distributed random number, which is given by the Fortran 90 random number generator; and K_h is the eddy diffusion
179 coefficient of the horizontal random walk, which is derived from the hydrodynamic model.

180 **2.2.2.3 Settling & resuspension related to MP shape factor**

181 The key behavioral description of MP particles is based on their shape, density, and size factor-dominated
182 settling and resuspension parameters. The settling and rising velocities (w_x) were calculated according to

183 $$w_x = \sqrt{\frac{4}{3}\frac{D_{eqv}^3}{d_{eq}^2 C_D}\left|\frac{\rho_m - \rho}{\rho}\right| g} \quad (2)$$

184 $$D_{eqv} = \sqrt[3]{abc} \quad (3)$$

185 where a, b, and c are the longest, intermediate and shortest lengths of MP particles, respectively; D_{eqv} is the
186 measured volume equivalent diameter; $d_{eq} = \sqrt{4ab/\pi}$ is the equivalent diameter; g is the gravitational acceleration;

187 C_D is the Stokes' drag coefficient that determines the settling or rise of MP particles; w_x is the settling (w_s) or rise

188 (w_r) velocity dependent on C_D; ρ_m is the density of specific MP, PP = 0.91 g/cm^3, initial PE = 0.95 g/cm^3 (Liu et

189 al., 2022); and ρ is the density of fluid.

190 For PP MPs, the particle density varied with time and was calculated using:

191 $$\rho_m = \frac{m_p + m_b}{V_p + V_b} \quad (4)$$

192 For settling to all shapes:

193 $$C_D = \frac{58.58ASF^{0.1936}}{Re^{0.8273}} \quad (5-1)$$

194 For rise to fiber:

195 $$C_{D,r,fibre} = \left(\frac{10}{\sqrt{Re}} + \sqrt{CSF}\right) \quad (5-2)$$

196 For rise to non-fiber:

197 $$C_{D,r,film} = \left(\frac{20 + 10\sqrt{Re}}{Re} + \sqrt{1.195 - CSF}\right) \times \left(\frac{6}{P}\right)^{1-CSF} \quad (5-3)$$

198 $$ASF = \frac{ac}{b^2}, CSF = \frac{c}{\sqrt{ab}}, Re = \frac{u_{t,mea} d_{eq}}{\nu} \quad (5-4)$$

199 where m_p and V_p are the initial mass and volume of PP MP; m_b and V_b are the mass and volume of biofilm;

200 $\rho_b = m_b/V_b$ =1.2 g/cm^3, density of biofilm according to (Amaral-Zettler et al., 2021; Van Melkebeke et al., 2020);

201 ASF is Aschenbrenner shape factor (Zhang and Choi, 2022); *CSF* is Corey shape factor (Waldschlaeger and

202 Schuettrumpf, 2019); Re is Reynolds number, ν is the kinematic viscosity of fluid (Kooi et al., 2017); P is the

203 power index, taking an average value of 1.95 for the film (Van Melkebeke et al., 2020). In our previous study (Shen

204 et al., 2022), more than 80% of the MPs carried by terrestrial runoff were stranded in the intertidal zones of

205 Chongming Island during the non-flood season, possibly because of the gentle topography and loose substrate

206 (Biltcliff-Ward et al., 2022; Diaz-Jaramillo et al., 2021). Therefore, the YRE intertidal zone with high MP

207 accumulation (Jiang et al., 2018; Long et al., 2021) should be a non-negligible MP provider (Fig. 2b) when a strong

runoff season occurs.

$$p_R = 1 - \exp\left(-\frac{\Delta t}{260 w_r + 7.1}\right) \quad (6)$$

where p_R is the probability of stranded MP particles being resuspended for a time step Δt synchronized with particle tracking module. A linear relationship between the MP rise velocity w_r (Eqs. 2, 5-1, and 5-3) and the resuspension time scale in days were acquired from Hinata et al. (2017). This formulation treats the p_R as a stochastic process and assumes that the main drivers of plastic stranding are the surface flow and input location. Next, regionally dominant MP types can be used as experimental particles to develop MP critical shear stresses that consider sediment particle size, density, and other parameters to accurately characterize the MP entrainment process.

2.3 Data acquisition

The use of multisource data is essential for calibrating numerical simulations and excluding outliers. First, hydrological data were obtained through regular monitoring by the Hydrological and Water Resources Survey Bureau of the YRE (Fig. 1). Hourly water level and salinity data were available for the four monitoring sections: NB, SB, NC, and SC. The XLJ monitoring station before the branch was equipped with four buoys with an Acoustic Doppler Current Profiler, GPS, OBS-3A turbidity meter, GPRS terminal, and digital radio to send real-time data to the central station every half hour, including current velocity, current direction, temperature, salinity, turbidity, and water level. The Tiler Map downloader (http://www.arctiler.com/) provided the initial data for the topography and bathymetry adopted in the model. Water level data for the sea boundary and background salinity values were provided by the China National Ocean Data Center (http://mds.nmdis.org.cn/). For areas with both monitored and collected data, the average values were used.

2.4 Hydrodynamic configuration

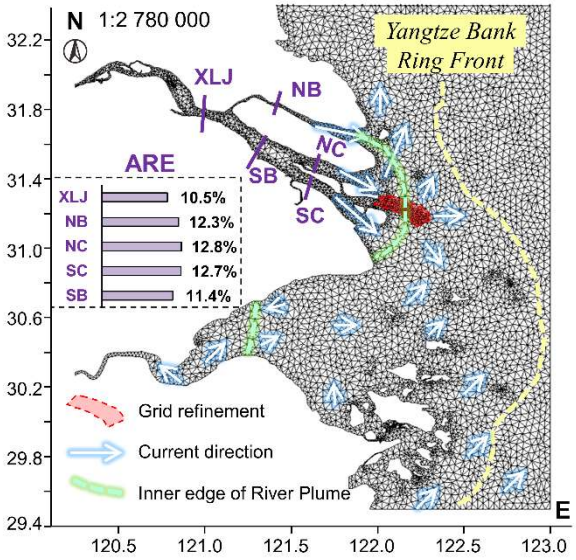

Fig. 3. Model meshes and locations of key hydrodynamic factors in the YRE. Purple columns represent the average relative error (ARE) of the water level in the main branch of the Yangtze River; white arrows represent the direction and speed of the current.

Hydrodynamics mainly drives the transport of MPs, with a small proportion (7%) determined by the MP properties (Wang et al., 2023b). The simulation configuration with a total area of 4.08×10^4 km^2 ensures accuracy by making the hydrodynamic module conform to the actual conditions of the YRE. As shown in Fig. 3, there are 10,864 triangular elements and 6,648 nodes employed as the fundamental structure, encompassing the mesh refinement required for the construction of a deepwater navigation channel project in NP. Three inlet boundaries (Yangtze River, Huangpu, and Qiantang) and three outlet boundaries of the North, East, and South Seas were available and their elevations were unified using Wusong data. The simulation for each scenario started from 00:00 on July 1, 2017, to 23:00 on July 31, 2017. The computational time step was dynamically adjusted to 1 min, depending on the grid size and water depth, to ensure that the Courant-Friedrich-Levy number was < 0.8, satisfying computational stability. The Manning number varied from $50\ m^{\frac{1}{3}}/s$ in the channel to $30\ m^{\frac{1}{3}}/s$ in the marsh according to (Attari and Hosseini,

2019). Based on the current field in July (Yuan et al., 2016) and the inner boundary of the river plume (Hickox et al., 2000; Wang et al., 2007) overlapping with the meshes, the YRP dominates the surface layer. The Qiantang River plume is confined to Hangzhou Bay, whereas the inner boundary of the nearshore front lies between 122.5–123.0 E (Hickox et al., 2000; Lee et al., 2015). Thus, the regional configuration covers the main hydrodynamic elements of the YRE. As a key indicator for simulation accuracy, the average relative error (ARE=$\frac{1}{n}\sum_{i=1}^{n}|Calculated - Measured|/Measured$) of water level in XLJ, NB, SB, NC, and SC sections were 10.54–12.79%, with a total average of 11.95%, as shown in Figs. S1-S5.

3. Results and discussion

3.1 Comparison of shape-dependent MP transport and source setting scenarios

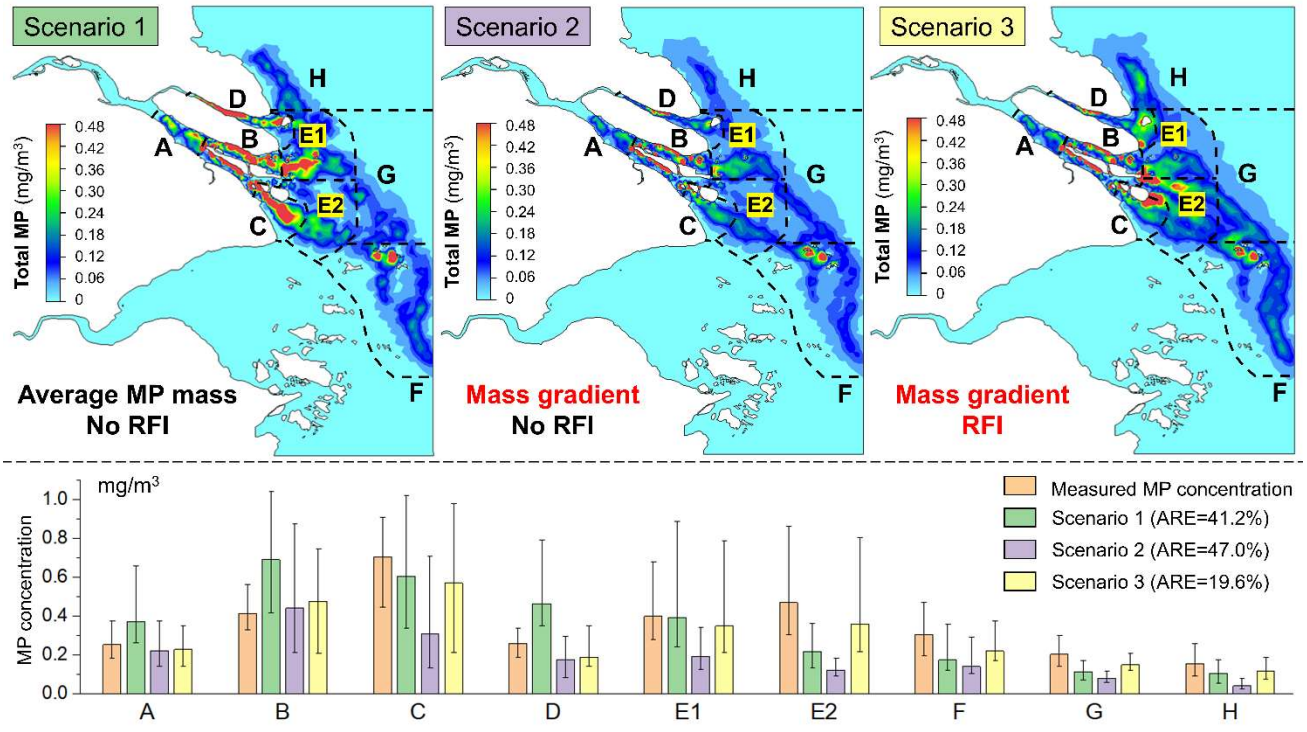

Fig. 4. Simulated surface MP distribution under three setting scenarios related to MP particle shape & source in the YRE: A: SB reach; B: NC reach; C: SC and SP reach; D: NB reach; E1: Confluence of NB and NC; E2 Confluence of SP and NP; F: South sea zone; G: East sea zone; H: North sea zone.

Compared to the converted measured mass concentrations (Zhao et al., 2019) (Fig. 4, measured MP concentration), zones A, B, and D, located in the inner estuary, presented a significant overestimation in Scenario 1 (ARE = 61.1%) and only 18.7% in Scenario 2. A reduction of over 40% proves that the adoption of particle mass gradients is beneficial for modeling the MP load of river inputs. However, the simulation of Scenario 1 performed better in the confluence zones of branching rivers. The median MP mass concentration in E1 reached 0.398 mg/m^3, with a relative error of only 1.3% of the measured value. Nevertheless, when transported to the sea zone (F, G, and H) near the estuarine front, the MPs of both scenarios were seriously underestimated. Preliminary judgments were obtained by combining the two scenarios. First, the adoption of a mass gradient facilitated the simulation of the riverine MP load, which was directly related to the accuracy of the MP mass concentration in the inner estuary. Secondly, the minor errors for E1 and E2 in Scenario 1 were largely attributed to an inflated mass concentration arising from the high average particle mass, which was an order of magnitude lower than the measured value when converted to the particle number. In the offshore zone, the falsely high MP particle mass did not mask the low number of releases (ARE = 39.7%). Therefore, the particle mass gradient was maintained in Scenario 3 while adding MP area sources released from Chongming Island, Changxing Island, and the Shanghai Jiuduansha Wetland National Nature Reserve (SJWNNR) (Fig. 2b), according to our simulated accumulation-prone zones in May 2017 (Shen et al., 2022).

From Fig. 4, it can be seen that Scenario 3 followed the low-error advantage of Scenario 2, with an ARE of 14.7% in the inner river channel (A, B, D). The MPs in NC mostly accumulated in the intertidal zone of eastern Chongming Island, resulting in a median mass concentration of 0.475 mg/m^3 in zone B, which was approximately 2.1 times that in zone A. The median mass concentration in zone C increased to 0.569 mg/m^3, which was the highest among all the zones, owing to the supplementation of intertidal particles from the SJWNNR. Although the ARE was still 5.1% higher than that in Scenario 1, it filled in the missing diversity in particle origin and quality. More remarkably, the

intertidal zone complemented the hotspots of MP accumulation in E1 and E2, increasing the median concentration in E2 by 0.141 mg/m^3 compared with Scenario 1. Although still approximately 26.6% lower than the measured median value in Zones F, G, and H, the ARE decreased significantly by 13.5% and 36.8% in Scenario 3 compared to those in Scenarios 1 and 2, respectively. Overall, the simulation results of Scenario 3 (ARE=19.6%) conformed to the MP distribution trend of the summer in the YRE: a gradual increase from upstream to downstream, with several MP hotspots in zones C, E1, and E2, followed by a gradual decrease. The distribution boundary of the low mass concentration of MPs (~0.06 mg/m^3) overlapped significantly with the location of the Yangtze Bank Ring Front (Fig. 2), which sufficiently corresponds to the retention effect by the estuarine front (Hickox et al., 2000; Wang et al., 2022; Wang et al., 2007).

3.2 Dominant MP type distribution and load modification in the surface of the YRE

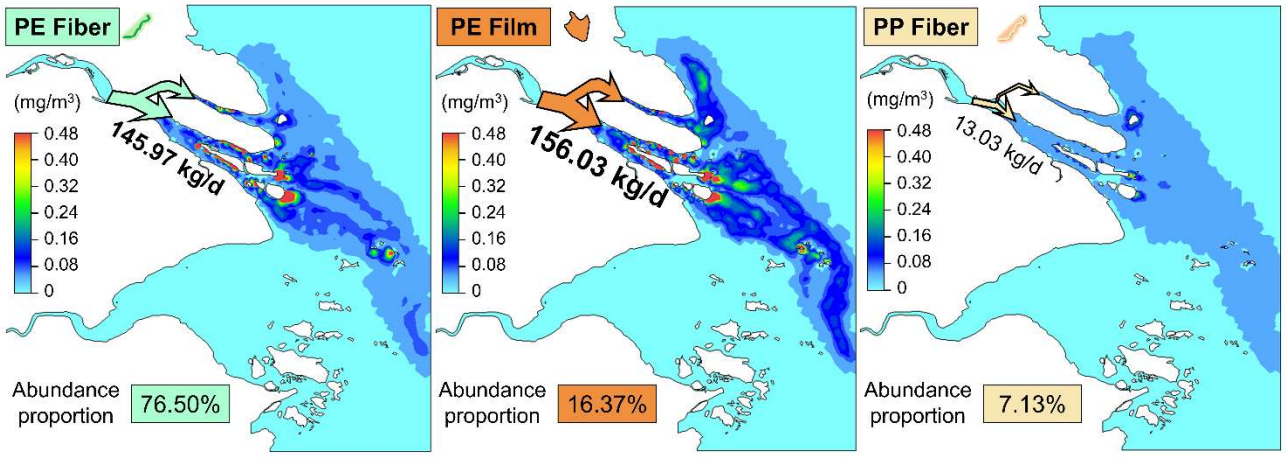

Fig. 5. Concentration of dominant MP types and daily MP load through the surface layer of the YRE estimated under Scenario 3

Scenario 3 controlled the ARE to < 20% and the sub-classified simulation assisted in understanding the differences between the transport and contribution of the main MP types. As indicated in Fig. 5, the PE fiber leads to three types of abundance (76.50% of the total) but its daily average input load (16.37%) is lower than that of the PE

292 film. PP fiber ranked last, with 7.13% abundance and 13.03 kg/d daily average input load. PE film provided nearly
293 50% of the input load with less than 17% of the quantity because the broad and flat shape characteristics of the film
294 resulted in a higher individual particle mass. As can be seen from SI2, the longest length (a) and intermediate length
295 (b) of the film usually remain within one order of magnitude, much longer than the shortest length (c). Therefore, the
296 mass of the film under the same size classification conditions is an order of magnitude higher than that of the fiber
297 and is easily represented parametrically by ASF < 0.1 (Zhang and Choi, 2022).

298 It is noteworthy that with guaranteed simulation accuracy, there is still an order of magnitude difference between
299 our estimated MP input loads and the results from Zhao et al. (2019). We identified a 10-fold increase in their
300 calculations. Zhao et al. (2019) estimated the average discharge through the YRE in summer to be 1206.2×10^9
301 m^3/month and the total surface MP mass to be 314.2 tons, which converted to 3415.22 kg/d. According to the Yangtze
302 River Sediment Bulletin, the average discharge at the Datong station should be about 1206.2×10^8 m^3/month
303 (http://www.cjw.gov.cn/UploadFiles/zwzc/2018/8/201808271416045463.pdf) in the summer of 2017. After
304 excluding this issue, the MP load calculated by Zhao et al., 2019 employing the empirical average particle mass (33
305 µg) was 341.52 kg/d, whereas the sum of our three main types was 315.03 kg/d. This difference lies mainly in the
306 estimation of particle mass. As can be seen from Table 1, 33 µg fell in the size fraction >1000 µm. The small particle
307 size PE fiber (60–500 µm), which accounts for nearly 43% of the total, had a much lower mass than 1 µg. The above
308 comparison demonstrates the need to estimate the multilevel mass of MP particles.

309 Furthermore, some limitations of this estuarine model must be overcome. Although the Yangtze River plume
310 and estuarine fronts dominate YRE current relationships, there may still be some interactions with the YRE in the
311 offshore region from the Zhejiang and Fujian coastal currents and the Taiwan Warm Current carrying MPs (~9 N/m^3)
312 from the Great Pacific Garbage (Egger et al., 2020; van Sebille et al., 2012; Wang et al., 2022). This may also account

for the low abundance of the sea zone (F, G, and H) simulations, where a reasonable setting of the boundary source, including atmospheric dry deposition, is worth careful research. Second, random errors in MP types with very low contents may be further amplified by errors present in the hydrodynamic simulations, thereby increasing the simulation uncertainty in MP transport. To achieve conciseness of the simulations, MPs that make up < 6%, of abundance were replaced with the three main MP types. However, differences in the polymer and shape combinations of these MP types to the three types used in the study may also contribute to transport errors, such as polyvinyl chloride fibers (1.46%) and polypropylene films (1.45%). It is possible to propose a confidence level applicable to MP classification simulations, which is referred to as the true classification coverage of MPs. For instance, this coverage can be set to 90% or 95%, depending on the accuracy requirements; however, the higher the value, the better. The remaining portion can be considered for equal scaling or developing a comprehensive alternative particle.

Moreover, the influence of substances in the near sea on MP transport also governs modeling accuracy. For example, recent studies found that nanobubbles generated by wave breaking and sheering not only bind to MPs, causing an increase in the measured mean particle size and concentration (Wang et al., 2023a) but also indirectly affect MP distributions by altering parameters such as surface tension (Xue et al., 2022). The next optimization focus will be to prepare experiments of the nanobubble-MP interaction (Jannesari et al., 2018) according to the regional hydrodynamic conditions to improve the settings of parameters such as the particle sinking rate and diffusion in the model. Overall, this study is the first application of estuarine MP simulations that highlights the importance of the PDF size for MP quantification (Koelmans et al., 2022; Kooi and Koelmans, 2019), which provides robust methodological support for accurately capturing the diffusion behavior for the entry of surface MPs into the sea.

3.3 Risk assessment combined with the MP abundance, shape, and polymer type

Existing risk assessment systems are generally based on MP abundance, shape, and polymer hazards. For

example, the pollution load index (PLI) is only positively correlated with MP abundance (Li et al., 2020a; Neelavannan et al., 2022). Based on the results extracted from the simulation, we combined the environmental status index (ESI) (Abelouah et al., 2022) with the Hazard Score (H) (Xu et al., 2018) to analyze the joint risk of various MP abundances, shapes, and polymer types in the water sources and nature reserves of the YRE. The comprehensive method was named the polymer-shape index (PSI) to compare the risk-discriminatory ability with the PLI. The process of combining all the above MP risk formulas and the PSI is presented in Text S1.

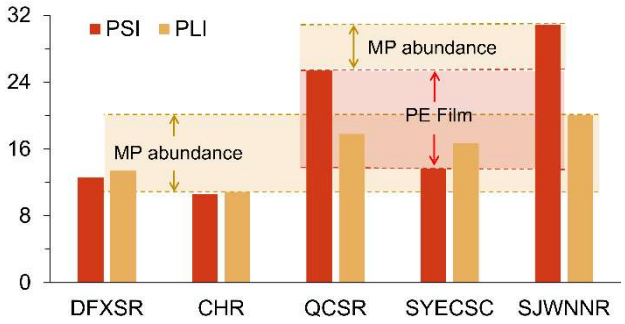

Fig. 6. Comparison of feature coverage capabilities in the risk assessment between PSI and PLI

When evaluated using PLI, QCSR, SYECSC, and SJWNNR showed higher risk values than CHR and DFXSR (Fig. 6), which aligned with the distribution of MPs in the YRE. Specifically, the abundance gradually increased downstream of the SB in the main river channel, forming aggregation hotspots in the confluence zones of the tributaries (E1 and E2) (Fig. 3, Scenario 3). In addition, DFXSR and CHR exhibited similar PSI and PLI values, reflecting the rationality of the PSI design. The ESI formula combines the functions of ESI and H (Table S6), which typically range from 1 to 4. Most MP polymers in the surface waters of the YRE are PP (H=11) and PE (H=5) (Frere et al., 2017; Zhang et al., 2020; Zheng et al., 2019), rather than types emerging with orders of magnitude differences in H values (Table S5), such as PVC, PUR, and ABS. Therefore, the low-risk range set by PSI (0–10) fits well with the PLI (Text S1).

Notably, in contrast to the significant increase in QCSR and SJWNNR, the PSI of SYECSC showed a slight

352 decrease compared to that of PLI. This intriguing phenomenon cannot be explained solely by abundance, as
353 SYECSC is also close to MP hotspots. For the ESI criteria, the film score exhibited greater sensitivity to the
354 abundance ranges than the other shapes (Table S4). Even with a minimal difference of 10 N/m^3 in abundance,
355 SYECSC, QCSR, and SJWNNR demonstrated distinct shape-score gradients, leading to significant differences
356 between PSI and PLI. Additionally, SJWNNR exhibited a 5.5 higher PSI than QCSR, concurrently reflecting its
357 contribution to abundance. Overall, PSI enables the comprehensive quantification of the differences in MP risk
358 arising from shape, abundance, and polymer type, rendering it more sensitive to evaluation than PLI. Aspects such
359 as the rationality of threshold settings and the dynamic variation of weights require further detailed assessments.
360 For instance, there is an overweighting of abundance when evaluating the MP risk normalized by the Beta
361 Coefficient, considering that both the ESI and PLI are based on abundance (Huang et al., 2023). Furthermore, the
362 regional risk threshold concentration of the total environmental MPs should be adjusted by obtaining the ingestible
363 size fraction of MPs and size-dependent cytotoxicity, such as oxidative stress and chromosomal aberrations
364 (Akhavan et al., 2012; Li et al., 2021). In addition, mesoscopic simulations combined with microscopic analyses,
365 such as SEM-EDS, XRF, or XRD, should be considered to explore the morphology of MPs and the level of pollutant
366 adsorption, updating the risk perception of MPs at the parameterized level. In summary, the development of a
367 classified tracking tool for riverine MPs could provide developing countries with a shared network that can be
368 continuously improved through collaboration. This will undoubtedly help comprehensively estimate MP loads,
369 locate the extent of MP aggregation hotspots, and more effectively remove MPs entering the sea globally. In the
370 future, this could also provide a basis for clarifying the traceability and responsibility division of emission reductions
371 for MPs in transnational rivers.

4. Conclusion

This study introduced a novel approach to correct MP input loadings by combining the size probability density function and shape classification through mass gradient calculations, replacing the conventional reliance on the average empirical particle mass. An improved drag model based on the ASF was applied to enhance the simulation of MP transport, with an average relative error of 19.6%. Furthermore, we developed a comprehensive risk assessment index that integrates MP shape, abundance, and polymer type using existing methods. This study improved the performance of MP simulation by addressing the problem of particle oversimplification from the full-process perspective of MP input, motion behavior, and cumulative risk analysis. The system provides a visual reference for tracking MPs in various water bodies, especially for characterizing their seaward environmental fate. By implementing more effective removal policies in estuaries, this model constitutes a low-cost measure to contribute to the reduction of the accumulation of global MP marine pollution.

Declaration of interest

None

Acknowledgment

This research was supported by the National Natural Science Foundation of China (No. 52179064), the Fundamental Research Funds for the Central Universities, the World - Class Universities (Disciplines), and the Characteristic Development Guidance Funds for the Central Universities, a project funded by the Priority Academic Program Development of Jiangsu Higher Education Institutions (No. 51479064). We acknowledge the support of the National Science & Technology Resource Sharing Service Platform of China, the National Meteorological Science Center, and NOAA's National Centers for Environmental Information. We sincerely thank Miss Mao Zhuyun for her selflessness, which helped to improve the linguistic quality of the manuscript.

Reference

Abelouah, M.R., Ben-Haddad, M., Rangel-Buitrago, N., Hajji, S., El Alem, N. and Alla, A.A. 2022. Microplastics pollution along the central Atlantic coastline of Morocco. Mar. Pollut. Bull. 174.

Akhavan, O., Ghaderi, E. and Akhavan, A. 2012. Size-dependent genotoxicity of graphene nanoplatelets in human stem cells. Biomaterials 33(32), 8017-8025.

Akhavan, O., Ghaderi, E. and Esfandiar, A. 2011. Wrapping Bacteria by Graphene Nanosheets for Isolation from Environment, Reactivation by Sonication, and Inactivation by Near-Infrared Irradiation. Journal of Physical Chemistry B 115(19), 6279-6288.

Akhavan, O., Ghaderi, E., Hashemi, E. and Akbari, E. 2015. Dose-dependent effects of nanoscale graphene oxide on reproduction capability of mammals. Carbon 95, 309-317.

Amaral-Zettler, L.A., Zettler, E.R., Mincer, T.J., Klaassen, M.A. and Gallager, S.M. 2021. Biofouling impacts on polyethylene density and sinking in coastal waters: A macro/micro tipping point? Water Research 201.

Andersen, T.J., Rominikan, S., Olsen, I.S., Skinnebach, K.H. and Fruergaard, M. 2021. Flocculation of PVC Microplastic and Fine-Grained Cohesive Sediment at Environmentally Realistic Concentrations. Biological Bulletin 240(1), 42-51.

Attari, M. and Hosseini, S.M. 2019. A simple innovative method for calibration of Manning's roughness coefficient in rivers using a similarity concept. J. Hydrol. 575, 810-823.

Besseling, E., Redondo-Hasselerharm, P., Foekema, E.M. and Koelmans, A.A. 2019. Quantifying ecological risks of aquatic micro- and nanoplastic. Critical Reviews in Environmental Science and Technology 49(1), 32-80.

Biltcliff-Ward, A., Stead, J.L. and Hudson, M.D. 2022. The estuarine plastics budget: A conceptual model and meta-analysis of microplastic abundance in estuarine systems. Estuar. Coast. Shelf Sci. 275.

Boucher, J. and Friot, D. 2017 Primary microplastics in the oceans: A global evaluation of sources.

Ceccarini, A., Corti, A., Erba, F., Modugno, F., La Nasa, J., Bianchi, S. and Castelvetro, V. 2018. The Hidden Microplastics: New Insights and Figures from the Thorough Separation and Characterization of Microplastics and of Their Degradation Byproducts in Coastal Sediments. Environ. Sci. Technol. 52(10), 5634-5643.

Celis-Hernandez, O., Cundy, A.B., Croudace, I.W., Ward, R.D., Busquets, R. and Wilkinson, J.L. 2021. Assessing the role of the "estuarine filter" for emerging contaminants: pharmaceuticals, perfluoroalkyl compounds and plasticisers in sediment cores from two contrasting systems in the southern UK. Water Research 189.

Chen, H., Jia, Q., Zhao, X., Li, L., Nie, Y., Liu, H. and Ye, J. 2020. The occurrence of microplastics in water bodies in urban agglomerations: Impacts of drainage system overflow in wet weather, catchment land-uses, and environmental management practices. Water Research 183.

Cohen, J.H., Internicola, A.M., Mason, R.A. and Kukulka, T. 2019. Observations and Simulations of Microplastic Debris in a Tide, Wind, and Freshwater-Driven Estuarine Environment: the Delaware Bay. Environ. Sci. Technol. 53(24), 14204-14211.

Collins, C. and Hermes, J.C. 2019. Modelling the accumulation and transport of floating marine micro-plastics around South Africa. Mar. Pollut. Bull. 139, 46-58.

Corlett, W.B. and Geyer, W.R. 2020. Frontogenesis at Estuarine Junctions. Estuaries Coasts 43(4), 722-738.

DHI (2017a) MIKE 3 Flow Model FM: Particle Tracking Module, User Guide, Danish Hydraulic Institute Water and Environment, Hørsholm, Denmark.

DHI (2017b) MIKE 21 & MIKE 3 Flow Model FM – Hydrodynamic and Transport Module, Scientific Documentation, Danish Hydraulic Institute Water and Environment, Hørsholm, Denmark.

Diaz-Jaramillo, M., Islas, M.S. and Gonzalez, M. 2021. Spatial distribution patterns and identification of microplastics

435 on intertidal sediments from urban and semi-natural SW Atlantic estuaries. Environ. Pollut. 273.
436 Durr, H.H., Laruelle, G.G., van Kempen, C.M., Slomp, C.P., Meybeck, M. and Middelkoop, H. 2011. Worldwide
437 Typology of Nearshore Coastal Systems: Defining the Estuarine Filter of River Inputs to the Oceans. Estuaries
438 Coasts 34(3), 441-458.
439 Egger, M., Sulu-Gambari, F. and Lebreton, L. 2020. First evidence of plastic fallout from the North Pacific Garbage
440 Patch. Scientific Reports 10(1).
441 Frere, L., Paul-Pont, I., Rinnert, E., Petton, S., Jaffre, J., Bihannic, I., Soudant, P., Lambert, C. and Huvet, A. 2017.
442 Influence of environmental and anthropogenic factors on the composition, concentration and spatial distribution
443 of microplastics: A case study of the Bay of Brest (Brittany, France). Environ. Pollut. 225, 211-222.
444 Geyer, R., Jambeck, J.R. and Law, K.L. 2017. Production, use, and fate of all plastics ever made. Science Advances
445 3(7).
446 He, S., Jia, M., Xiang, Y., Song, B., Xiong, W., Cao, J., Peng, H., Yang, Y., Wang, W., Yang, Z. and Zeng, G. 2022.
447 Biofilm on microplastics in aqueous environment: Physicochemical properties and environmental implications. J.
448 Hazard. Mater. 424.
449 Hermabessiere, L., Dehaut, A., Paul-Pont, I., Lacroix, C., Jezequel, R., Soudant, P. and Duflos, G. 2017. Occurrence
450 and effects of plastic additives on marine environments and organisms: A review. Chemosphere 182, 781-793.
451 Hickox, R., Belkin, I., Cornillon, P. and Shan, Z. 2000. Climatology and seasonal variability of ocean fronts in the east
452 China, Yellow and Bohai Seas from satellite SST data. Geophys. Res. Lett. 27(18), 2945-2948.
453 Hinata, H., Mori, K., Ohno, K., Miyao, Y. and Kataoka, T. 2017. An estimation of the average residence times and
454 onshore-offshore diffusivities of beached microplastics based on the population decay of tagged meso- and
455 macrolitter. Mar. Pollut. Bull. 122(1-2), 17-26.
456 Huang, Q.e., Liu, M., Cao, X. and Liu, Z. 2023. Occurrence of microplastics pollution in the Yangtze River: Distinct
457 characteristics of spatial distribution and basin-wide ecological risk assessment. Water Research 229, 119431.
458 Hurley, R., Woodward, J. and Rothwell, J.J. 2018. Microplastic contamination of river beds significantly reduced by
459 catchment-wide flooding. Nature Geoscience 11(4), 251-+.
460 Jalon-Rojas, I., Wang, X.H. and Fredj, E. 2019. A 3D numerical model to Track Marine Plastic Debris (TrackMPD):
461 Sensitivity of microplastic trajectories and fates to particle dynamical properties and physical processes. Mar.
462 Pollut. Bull. 141, 256-272.
463 Jambeck, J.R., Geyer, R., Wilcox, C., Siegler, T.R., Perryman, M., Andrady, A., Narayan, R. and Law, K.L. 2015. Plastic
464 waste inputs from land into the ocean. Science 347(6223), 768-771.
465 Jannesari, M., Akhavan, O. and Madaah Hosseini, H.R. 2018. Graphene oxide in generation of nanobubbles using
466 controllable microvortices of jet flows. Carbon 138, 8-17.
467 Jiang, P., Zhao, S., Zhu, L. and Li, D. 2018. Microplastic-associated bacterial assemblages in the intertidal zone of the
468 Yangtze Estuary. Sci. Total Environ. 624, 48-54.
469 Jin, H., Yan, M., Pan, C., Liu, Z., Sha, X., Jiang, C., Li, L., Pan, M., Li, D., Han, X. and Ding, J. 2022. Chronic exposure
470 to polystyrene microplastics induced male reproductive toxicity and decreased testosterone levels via the LH-
471 mediated LHR/cAMP/PKA/StAR pathway. Particle and Fibre Toxicology 19(1), 13.
472 Koelmans, A.A., Besseling, E., Foekema, E., Kooi, M., Mintenig, S., Ossendorp, B.C., Redondo-Hasselerharm, P.E.,
473 Verschoor, A., van Wezel, A.P. and Scheffer, M. 2017. Risks of Plastic Debris: Unravelling Fact, Opinion,
474 Perception, and Belief. Environ. Sci. Technol. 51(20), 11513-11519.
475 Koelmans, A.A., Redondo-Hasselerharm, P.E., Nor, N.H.M., de Ruijter, V.N., Mintenig, S.M. and Kooi, M. 2022. Risk
476 assessment of microplastic particles. Nature Reviews Materials 7(2), 138-152.
477 Kooi, M. and Koelmans, A.A. 2019. Simplifying Microplastic via Continuous Probability Distributions for Size, Shape,

and Density. Environmental Science & Technology Letters 6(9), 551-557.
Kooi, M., Primpke, S., Mintenig, S.M., Lorenz, C., Gerdts, G. and Koelmans, A.A. 2021. Characterizing the multidimensionality of microplastics across environmental compartments. Water Research 202.
Kooi, M., van Nes, E.H., Scheffer, M. and Koelmans, A.A. 2017. Ups and Downs in the Ocean: Effects of Biofouling on Vertical Transport of Microplastics. Environ. Sci. Technol. 51(14), 7963-7971.
Lagarde, F., Olivier, O., Zanella, M., Daniel, P., Hiard, S. and Caruso, A. 2016. Microplastic interactions with freshwater microalgae: Hetero-aggregation and changes in plastic density appear strongly dependent on polymer type. Environ. Pollut. 215, 331-339.
Lebreton, L.C.M., Van der Zwet, J., Damsteeg, J.-W., Slat, B., Andrady, A. and Reisser, J. 2017. River plastic emissions to the world's oceans. Nature Communications 8.
Lee, M.-a., Chang, Y. and Shimada, T. 2015. Seasonal evolution of fine-scale sea surface temperature fronts in the East China Sea. Deep-Sea Research Part Ii-Topical Studies in Oceanography 119, 20-29.
Li, L., Geng, S., Wu, C., Song, K., Sun, F., Visvanathan, C., Xie, F. and Wang, Q. 2019. Microplastics contamination in different trophic state lakes along the middle and lower reaches of Yangtze River Basin. Environ. Pollut. 254.
Li, R., Yu, L., Chai, M., Wu, H. and Zhu, X. 2020a. The distribution, characteristics and ecological risks of microplastics in the mangroves of Southern China. Sci. Total Environ. 708.
Li, Y., Lu, Z., Zheng, H., Wang, J. and Chen, C. 2020b. Microplastics in surface water and sediments of Chongming Island in the Yangtze Estuary, China. Environmental Sciences Europe 32(1), 15.
Li, Z.L., Feng, C.H., Pang, W., Tian, C.H. and Zhao, Y. 2021. Nanoplastic-Induced Genotoxicity and Intestinal Damage in Freshwater Benthic Clams (Corbicula fluminea): Comparison with Microplastics. Acs Nano 15(6), 9469-9481.
Liu, S., Huang, Y., Luo, D., Wang, X., Wang, Z., Ji, X., Chen, Z., Dahlgren, R.A., Zhang, M. and Shang, X. 2022. Integrated effects of polymer type, size and shape on the sinking dynamics of biofouled microplastics. Water Research 220.
Long, J., Tong, C., Wang, T., Wu, F. and Liu, M. 2021. Distribution characteristics and influencing factors of microplastics in intertidal zone sediments of the Yangtze Estuary. Chinese Journal of Ecology 40(9), 2860-2871.
Long, M., Paul-Pont, I., Hegaret, H., Moriceau, B., Lambert, C., Huvet, A. and Soudant, P. 2017. Interactions between polystyrene microplastics and marine phytoplankton lead to species-specific hetero-aggregation. Environ. Pollut. 228, 454-463.
Luo, W., Su, L., Craig, N.J., Du, F., Wu, C. and Shi, H. 2019. Comparison of microplastic pollution in different water bodies from urban creeks to coastal waters. Environ. Pollut. 246, 174-182.
MacLeo, M., Arp, H.P.H., Tekman, M.B. and Jahnke, A. 2021. The global threat from plastic pollution. Science 373(6550), 61-65.
Meijer, L.J.J., van Emmerik, T., van der Ent, R., Schmidt, C. and Lebreton, L. 2021. More than 1000 rivers account for 80% of global riverine plastic emissions into the ocean. Science Advances 7(18).
Neelavannan, K., Sen, I.S., Lone, A.M. and Gopinath, K. 2022. Microplastics in the high-altitude Himalayas: Assessment of microplastic contamination in freshwater lake sediments, Northwest Himalaya (India). Chemosphere 290.
Obodoefuna, D.C., Fan, D., Guo, X. and Li, B. 2020. Highly accelerated siltation of abandoned distributary channel in the Yangtze Delta under everchanging social-ecological dynamics. Marine Geology 429, 106331.
Odonnell, J. 1993. SURFACE FRONTS IN ESTUARIES - A REVIEW. Estuaries 16(1), 12-39.
Onink, V., Jongedijk, C.E., Hoffman, M.J., van Sebille, E. and Laufkoetter, C. 2021. Global simulations of marine plastic transport show plastic trapping in coastal zones. Environmental Research Letters 16(6).
Onink, V., Kaandorp, M.L.A., van Sebille, E. and Laufkotter, C. 2022. Influence of Particle Size and Fragmentation on

Large-Scale Microplastic Transport in the Mediterranean Sea. Environ. Sci. Technol.

Peng, G.Y., Zhu, B.S., Yang, D.Q., Su, L., Shi, H.H. and Li, D.J. 2017. Microplastics in sediments of the Changjiang Estuary, China. Environ. Pollut. 225, 283-290.

Rummel, C.D., Jahnke, A., Gorokhova, E., Kuehnel, D. and Schmitt-Jansen, M. 2017. Impacts of Biofilm Formation on the Fate and Potential Effects of Microplastic in the Aquatic Environment. Environmental Science & Technology Letters 4(7), 258-267.

Schirinzi, G.F., Perez-Pomeda, I., Sanchis, J., Rossini, C., Farre, M. and Barcelo, D. 2017. Cytotoxic effects of commonly used nanomaterials and microplastics on cerebral and epithelial human cells. Environmental Research 159, 579-587.

Schmidt, C., Krauth, T. and Wagner, S. 2017. Export of Plastic Debris by Rivers into the Sea. Environ. Sci. Technol. 51(21), 12246-12253.

Shanghai Water Authority. 2020 Overview of surface water resources in Shanghai 2017. Available at https://swj.sh.gov.cn/shsdfssglc-fxpj/20200121/12b412d424544d72af6642c4da7d700d.html/ (Accessed 20 January 2020).

Shen, Z., Wang, H., Liang, D., Yan, Y. and Zeng, Y. 2022. The fate of microplastics in estuary: A quantitative simulation approach. Water Research 226.

Singh, N., Tiwari, E., Khandelwal, N. and Darbha, G.K. 2019. Understanding the stability of nanoplastics in aqueous environments: effect of ionic strength, temperature, dissolved organic matter, clay, and heavy metals. Environmental Science-Nano 6(10), 2968-2976.

Song, Y.K., Hong, S.H., Jang, M., Han, G.M., Jung, S.W. and Shim, W.J. 2017. Combined Effects of UV Exposure Duration and Mechanical Abrasion on Microplastic Fragmentation by Polymer Type. Environ. Sci. Technol. 51(8), 4368-4376.

Van Melkebeke, M., Janssen, C. and De Meester, S. 2020. Characteristics and Sinking Behavior of Typical Microplastics Including the Potential Effect of Biofouling: Implications for Remediation. Environ. Sci. Technol. 54(14), 8668-8680.

van Sebille, E., England, M.H. and Froyland, G. 2012. Origin, dynamics and evolution of ocean garbage patches from observed surface drifters. Environmental Research Letters 7(4).

Waldschlaeger, K. and Schuettrumpf, H. 2019. Effects of Particle Properties on the Settling and Rise Velocities of Microplastics in Freshwater under Laboratory Conditions. Environ. Sci. Technol. 53(4), 1958-1966.

Wang, T., Zha, S., Zhu, L., McWilliams, J.C., Galgani, L., Amin, R.M., Nakajima, R., Jiang, W. and Chen, M. 2022. Accumulation, transformation and transport of microplastics in estuarine fronts. Nature Reviews Earth & Environment 3(11), 795-805.

Wang, X., Bolan, N., Tsang, D.C.W., Sarkar, B., Bradney, L. and Li, Y. 2021. A review of microplastics aggregation in aquatic environment: Influence factors, analytical methods, and environmental implications. J. Hazard. Mater. 402, 123496.

Wang, Z., An, C., Lee, K. and Feng, Q. 2023a. Overlooked Role of Bulk Nanobubbles in the Alteration and Motion of Microplastics in the Ocean Environment. Environ. Sci. Technol. 57(30), 11289-11299.

Wang, Z., Li, L., Chen, D., Xu, K., Wei, T., Gao, J., Zhao, Y., Chen, Z. and Masabate, W. 2007. Plume front and suspended sediment dispersal off the Yangtze (Changjiang) River mouth, China during non-flood season. Estuarine, Coastal and Shelf Science 71(1), 60-67.

Wang, Z., Pilechi, A., Fok Cheung, M. and Ariya, P.A. 2023b. In-situ and real-time nano/microplastic coatings and dynamics in water using nano-DIHM: A novel capability for the plastic life cycle research. Water research 235, 119898-119898.

Weiss, L., Ludwig, W., Heussner, S., Canals, M., Ghiglione, J.-F., Estournel, C., Constant, M. and Kerhervé, P. 2021. The missing ocean plastic sink: Gone with the rivers. Science 373(6550), 107-111.

Wiesinger, H., Wang, Z. and Hellweg, S. 2021. Deep Dive into Plastic Monomers, Additives, and Processing Aids. Environ. Sci. Technol. 55(13), 9339-9351.

Woodward, J., Li, J., Rothwell, J. and Hurley, R. 2021. Acute riverine microplastic contamination due to avoidable releases of untreated wastewater. Nature Sustainability 4(9), 793-+.

Xu, P., Peng, G., Su, L., Gao, Y., Gao, L. and Li, D. 2018. Microplastic risk assessment in surface waters: A case study in the Changjiang Estuary, China. Mar. Pollut. Bull. 133, 647-654.

Xue, S., Zhang, Y., Marhaba, T. and Zhang, W. 2022. Aeration and dissolution behavior of oxygen nanobubbles in water. Journal of Colloid and Interface Science 609, 584-591.

Yin, K., Wang, Y., Zhao, H., Wang, D., Guo, M., Mu, M., Liu, Y., Nie, X., Li, B., Li, J. and Xing, M. 2021. A comparative review of microplastics and nanoplastics: Toxicity hazards on digestive, reproductive and nervous system. Sci. Total Environ. 774, 145758.

Yuan, R., Wu, H., Zhu, J. and Li, L. 2016. The response time of the Changjiang plume to river discharge in summer. J. Mar. Syst. 154, 82-92.

Yuan, W., Christie-Oleza, J.A., Xu, E.G., Li, J., Zhang, H., Wang, W., Lin, L., Zhang, W. and Yang, Y. 2022. Environmental fate of microplastics in the world's third-largest river: Basin-wide investigation and microplastic community analysis. Water Res 210, 118002.

Zhang, B., Yang, X., Liu, L., Chen, L., Teng, J., Zhu, X., Zhao, J. and Wang, Q. 2021. Spatial and seasonal variations in biofilm formation on microplastics in coastal waters. Sci. Total Environ. 770.

Zhang, J. and Choi, C.E. 2022. Improved Settling Velocity for Microplastic Fibers: A New Shape-Dependent Drag Model. Environ. Sci. Technol. 56(2), 962-973.

Zhang, L., Liu, J., Xie, Y., Zhong, S., Yang, B., Lu, D. and Zhong, Q. 2020. Distribution of microplastics in surface water and sediments of Qin river in Beibu Gulf, China. Sci. Total Environ. 708.

Zhao, S., Zhu, L., Wang, T. and Li, D. 2014. Suspended microplastics in the surface water of the Yangtze Estuary System, China: First observations on occurrence, distribution. Mar. Pollut. Bull. 86(1-2), 562-568.

Zhao, S.Y., Wang, T., Zhu, L.X., Xu, P., Wang, X.H., Gao, L. and Li, D.J. 2019. Analysis of suspended microplastics in the Changjiang Estuary: Implications for riverine plastic load to the ocean. Water Research 161, 560-569.

Zheng, Y., Li, J., Cao, W., Liu, X., Jiang, F., Ding, J., Yin, X. and Sun, C. 2019. Distribution characteristics of microplastics in the seawater and sediment: A case study in Jiaozhou Bay, China. Sci. Total Environ. 674, 27-35.

Zhou, X., Chen, L., Yang, J. and Wu, H. 2020. Chinese sturgeon needs urgent rescue. Science 370(6521), 1175-1175.